

# Self-Assembly of Cellulose Nanocrystals into Semi-Spherical Photonic Cholesteric Films

Pardis Rofouie, Moien Alizadehgiashi, Haridas Mundoor, Ivan I. Smalyukh, and Eugenia Kumacheva\*

Spherical-shape cholesteric (Ch) photonic films offer promising applications such as omnidirectional lasing and broadband reflection. Here, a strategy is reported for the fabrication of photonic Ch films by the self-assembly of cellulose nanocrystals (CNCs) in semi-spherical cavities. It is shown that film structure and photonic properties are controlled by the film curvature, the composition of the precursor CNC suspension, and its liquid crystalline or isotropic state. The effect of curvature of the drying Ch-CNC films coupled with the restricted mobility of CNCs during film preparation results in the variation in pitch and helical axis inclination, thus leading to broadband reflectance properties of the films. The role of curvature of the Ch-CNC films is underlined by comparing their distinct properties with those of planar films with the same composition. These findings provide a novel insight into the design and development of biomimetic photonic Ch films.

## 1. Introduction

Chirality is an essential characteristic in nature, which embraces a broad range of length scales from molecules (e.g., DNA<sup>[1]</sup> and proteins) to microfibrils (e.g., collagen filaments<sup>[2]</sup>) to macroscopic scales such as twisted plywood architecture in plant cell walls.<sup>[3]</sup> The cholesteric (Ch) structure is believed to be responsible for the remarkable strength and toughness,<sup>[4]</sup> and mechanical adaptability of biological materials, e.g., fish scale<sup>[5]</sup> and rabbit skin.<sup>[5,6]</sup> The Ch fibrillar morphology can also lead to greater material's fracture resistance, since the variation in fiber orientation from layer to layer diverts the path of crack propagation, resulting in an increased capacity to dissipate energy.<sup>[7]</sup> With respect to the optical properties of Ch films, selective reflection of light from multilayer structures is the origin of structural colors in plants,<sup>[8]</sup> insect cuticles,<sup>[9]</sup>

and fruits.<sup>[10]</sup> These structures act as Bragg's reflectors, in which the helical axis is perpendicular to the surface and the helix pitch  $P$  is in the spectral range from  $\approx 150$  nm to  $16 \mu\text{m}$ .<sup>[11]</sup> Structural coloration has a pivotal role in the evolution and survival of plants and fruits,<sup>[12]</sup> making them attractive to pollinators and birds.<sup>[13]</sup> Photonic structures in plants can also play a role in light management either by inhibiting ultraviolet radiation, or by focusing light on the chloroplasts. Furthermore, selective reflection of light can be coupled with absorption of light by pigments.<sup>[14]</sup> For example, light transmitted through epidermal cells in the fruit of *Polia condensata* is absorbed through multiple layers of cells containing brown


tannin pigment; the latter spectrally filters structural coloration and enhances the selective reflection.<sup>[8a]</sup>

The optical and mechanical properties of Ch biomaterials have inspired the design and fabrication of biomimetic materials with a Ch structure.<sup>[15]</sup> In particular, the ability of rod-like cellulose nanocrystals (CNCs) to form a Ch liquid crystalline phase in aqueous suspensions has attracted considerable interest of the materials science community.<sup>[16,17]</sup> Remarkably, the helicoidal CNC organization can be preserved in solid films,<sup>[18]</sup> with a pitch,  $P$ , being reduced from micrometers (in CNC suspensions) to hundreds of nanometers in films.<sup>[17,18]</sup> As a result, the CNC films exhibit structural colors and are iridescent.<sup>[15c,19]</sup> Light is selectively reflected at the wavelength  $\lambda = nP\sin\theta$ , where  $n$  is the average refractive index of the CNC film ( $n \approx 1.53$ )<sup>[20]</sup> and  $\theta$  is the angle of incidence of light with respect to the surface normal.<sup>[21]</sup> The Ch-CNC film strongly reflects left-handed circularly polarized light. Owing to their photonic properties, Ch-CNC films show promising applications in colorimetric humidity sensing,<sup>[16]</sup> optical encryption,<sup>[22]</sup> chiral plasmonics,<sup>[23]</sup> and light scattering shutters.<sup>[24]</sup> Notably, such materials represent an alternative to the thermotropic chiral nematic liquid crystals, due to the availability, low cost, sustainability, compatibility with water, and biocompatibility of CNCs.<sup>[25]</sup>

To achieve control over photonic and mechanical properties of Ch-CNC films, substantial efforts have been directed toward the exploration of the role of different factors on film structure, including the role of the CNC charge and concentration in the precursor aqueous suspension,<sup>[17]</sup> water evaporation rate,<sup>[26]</sup> wetting of the substrate,<sup>[27]</sup> temperature of film formation,<sup>[28]</sup>

Dr. P. Rofouie, M. Alizadehgiashi, Prof. E. Kumacheva  
Department of Chemistry  
University of Toronto  
80 Saint George Str., Toronto, Ontario M5S 3H6, Canada  
E-mail: ekumache@chem.utoronto.ca

Dr. H. Mundoor, Prof. I. I. Smalyukh  
Department of Physics  
Materials Science and Engineering  
and Renewable and Sustainable Energy Institute (RASEI)  
University of Colorado  
Boulder, CO 80309, USA

 The ORCID identification number(s) for the author(s) of this article can be found under <https://doi.org/10.1002/adfm.201803852>.

DOI: 10.1002/adfm.201803852

suspension sonication time,<sup>[28]</sup> the helical axis,<sup>[29]</sup> and addition of low- and high-molecular weight additives.<sup>[30]</sup> These studies have been restricted to the fabrication of planar CNC films.

The fabrication of Ch-CNC films that act as curved Bragg reflectors (e.g., similar to that in *Pollia condensata*<sup>[8a]</sup>) has not been reported. The combination of photonic properties and spherical geometry of these films can broaden the reflection bandwidth of the Ch-CNC films to overcome the restricted reflectance, a major limitation in the fabrication of broadband circular polarizers, broadband reflectors, and polarization-independent devices<sup>[31]</sup> and can lead to their applications in omnidirectional lasing,<sup>[32]</sup> autonomous sensing,<sup>[33]</sup> secure authentication,<sup>[34]</sup> and micro-optofluidics.<sup>[35]</sup> To explore the organization of CNCs in spherical confinement, spherical droplets,<sup>[36]</sup> and microgels<sup>[37]</sup> with a distinct Ch morphology have been generated from Ch-CNC suspensions. Unfortunately, these systems cannot be used for the preparation of high-quality spherical Ch films with a pitch,  $P$ , in the sub-micrometer range. First, under isotropic (omnidirectional) water evaporation conditions a significant reduction in  $P$  (from several micrometer to the sub-micrometer range) cannot be expected, as their linear dimensions of spherical droplets/microgels reduce as a cubic root of the volume. For example, a 95% reduction in droplet volume due to water evaporation leads to only 63% decrease in droplet radius, and complete isotropic water evaporation from, e.g., a 140  $\mu\text{m}$  diameter Ch-CNC droplet with CNC concentration,  $C_{\text{CNC}}$ , of 10 vol/vol% and  $P \approx 3 \mu\text{m}$ , would yield  $P \approx 1.5 \mu\text{m}$ .<sup>[38]</sup> Notably, for planar Ch-CNC films, evaporation of water from the same suspension reduces to  $P \approx 250 \text{ nm}$ .<sup>[38]</sup> Second, the evaporation of water from Ch-CNC droplets would cause surface buckling<sup>[38,39]</sup> and hence distortion of the Ch structure of the resulting films.

Here, we report the fabrication of semi-spherical Ch-CNC films by evaporating water from CNC suspensions placed in a semi-spherical template. This work elucidates the interplay between the spherical geometry, the composition of the precursor CNC suspension, and the Ch-CNC film structure and optical properties. Drying the CNC suspension in a template governed a semi-spherical shape of the Ch-CNC films and affected their thickness and structure due to the capillary, Marangoni, and gravity-driven flows. Site-specific properties of the films were controlled by the interplay of CNC organization in the films and shear imposed by the drying process. The Ch structure was preserved in curved films, with  $P$  being commensurate with the wavelengths in a visible spectral range. Owing to the planar CNC alignment at the CNC/air and CNC/substrate interfaces, the helical axis of the film was normal to its interfaces with air. Under particular conditions, the spherical geometry of the films promoted the formation of the polydomain structure and helix axis inclination, thus resulting in broadband reflectance spectra. This work offers a strategy toward the fabrication of Ch films with broad bandgap properties.

## 2. Fabrication of Ch-CNC Films

Figure 1 schemes the approach to the fabrication of Ch-CNC films with a semi-spherical shape. The transmission electron microscopy image of the negatively charged, rod-like CNCs with an average length and diameter of 176 and 21 nm is shown in Figure S1 in the Supporting Information. Custom-made glass semi-spheres with a radius  $R$  of 3 or 2 mm (corresponding to the curvature  $\kappa = 1/R$ , of 0.33 and 0.50  $\text{mm}^{-1}$ , respectively) were placed into two different 60  $\times$  15  $\text{mm}^2$  polystyrene Petri dishes, with a concave side of the semi-sphere facing the bottom of the dish (Figure 1a). Polydimethylsiloxane (PDMS) prepolymer and a curing agent (Sylgard 184, Dow Corning Corporation) mixed at a weight ratio of 10:1, respectively, was degassed, poured onto the semi-spheres with a PDMS layer being 2 mm above the top of the glass semi-spheres, and cured at 70  $^\circ\text{C}$  for 2 h (Figure 1b). The PDMS molds were peeled off and the glass semi-spheres were removed. To moderate hydrophobicity of the PDMS surface,<sup>[40]</sup> the molds were surface modified using air plasma treatment (3000 mTorr) for 120 s (the effect of PDMS plasma treatment on the contact angle of CNC dispersion and the configuration of the resultant film is shown in Figures S2 and S3, respectively, Supporting Information). After the plasma treatment, the semi-spherical cavities left in the PDMS mold after removing glass semi-spheres were filled with a suspension with a CNC concentration,  $C_{\text{CNC}}$ , and the mold was placed for 7 d into a chamber with a controlled relative humidity of  $\approx 80\%$  at 28  $^\circ\text{C}$  (Figure 1c). After water evaporation, the dry semi-spherical Ch-CNC films “caps” were detached from the PDMS mold (Figure 1d).

In this work, four types of CNC suspensions denoted isotropic (ISO)-3, ISO-7, ISO-6.7\_equilibrium phase (EQ), and chiral (Ch)-7.3\_EQ were used to fabricate the semi-spherical films (see Table 1). To reveal the role of curvature on optical properties of the semi-spherical films, planar films (P-ISO-3, P-ISO-7, P-ISO-6.7\_EQ, and P-Ch-7.3\_EQ) were prepared from the same CNC suspensions as the corresponding curved films (listed in

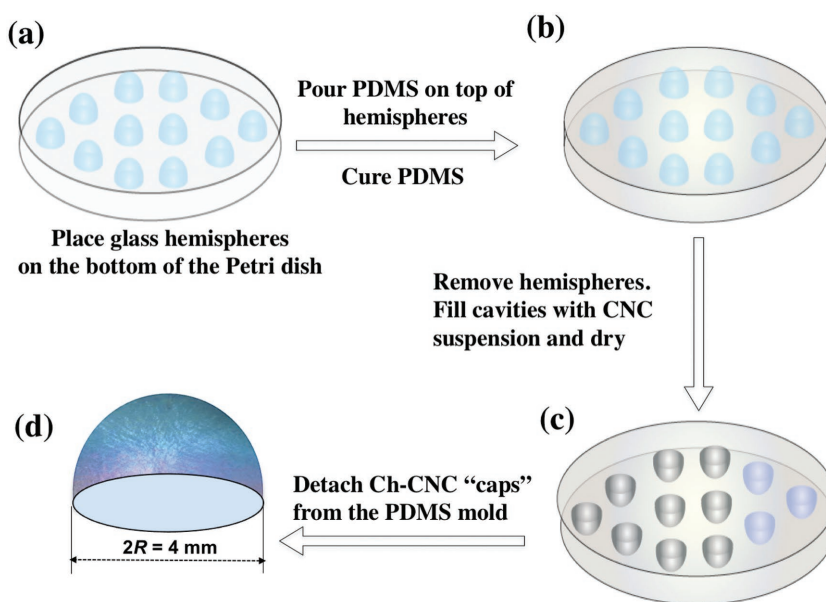


Figure 1. Schematic illustration of the fabrication of semi-spherical Ch-CNC shells.

**Table 1.** Composition and structures of CNC suspensions of the Ch curved films.

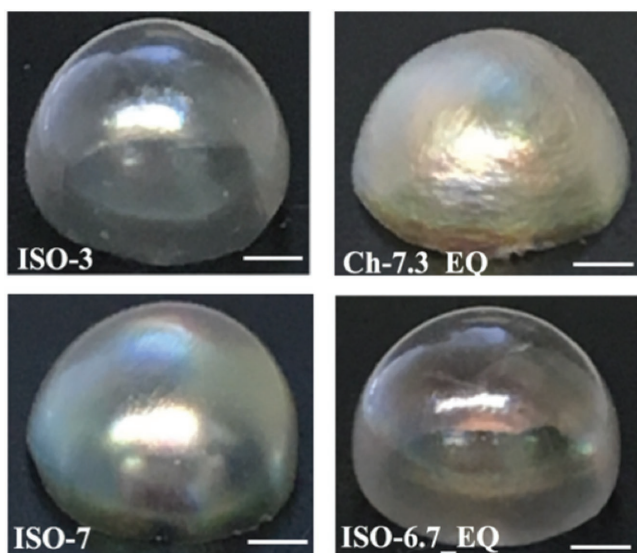
Film	C <sub>CNC</sub> in suspension [wt%]	Initial suspension state	Viscosity, $\eta$ [Pa s]
ISO-3 P-ISO-3	3.0	Isotropic	$0.031 \pm 0.005$
ISO-7 P-ISO-7	7.0	Isotropic	$0.250 \pm 0.009$
ISO-6.7_EQ P-ISO-6.7_EQ	6.7	Isotropic, after equilibration	$0.077 \pm 0.002$
Ch-7.3_EQ P-Ch-7.3_EQ	7.3	Cholesteric, after equilibration	$0.430 \pm 0.001$

Table 1). The film preparation was similar to the fabrication of the curved films.

### 3. Results

#### 3.1. Film Appearance

**Figure 2** shows representative photographs of four films with a radius  $R = 2$  mm, which were formed from the CNC suspensions listed in Table 1. Film inspection with optical microscopy showed no cracks and macroscopic defects. All the films displayed the iridescence. The ISO-3 and ISO-7 films showed reflection in the blue/green spectral range, whereas the ISO-6.7\_EQ and Ch-7.3\_EQ films exhibited red/yellow structural color. The ISO-7 and Ch-7.3\_EQ films exhibited a stronger metallic reflection than the ISO-3 and ISO-6.7\_EQ films. The Ch-7.3\_EQ film had a rough surface, in comparison with other films. Curved films with a radius  $R = 3$  mm that were prepared from the precursor suspensions listed in Table 1 showed a similar appearance (Figure S4, Supporting Information). We note that under optimized conditions of film preparation, the structure and film properties reported below were highly reproducible.



**Figure 2.** Photographs of the Ch-CNC films formed from suspensions listed in Table 1: ISO-3, ISO-7, ISO-6.7\_EQ, and Ch-7.3\_EQ films. All scale bars are 1 mm.

#### 3.2. Variation in Film Thickness

The relationship between the CNC concentration and the state of the precursor suspension and the Ch-CNC film thickness,  $d$ , and pitch,  $P$ , was studied by examining the scanning electron microscope (SEM) images of the film cross-section. **Figure 3a** illustrates a schematic of the film cross-section with the indication of nine examined locations on the right and left halves of the curved film. The points 1–5 on the right half of the “cap” were located on the film surface at a radius  $r = R$

and an azimuthal angle  $\phi = 90^\circ$  with a varying polar angle,  $\theta_n$ , where  $n$  denotes the position from 1 to 5 on the right half of the film. Positions 2'–5' on the left half of the film were located on the film surface at  $r = R$  and an azimuthal angle of  $\phi = 270^\circ$  with a varying polar angle,  $\theta_{n'}$ , where  $n'$  denotes the local point number from 2 to 5 on the left half of the film. These points are indicated in the SEM image of the cross-section of the ISO-7 film embedded into the epoxy resin (Figure 3b). The locations at  $\theta = 90^\circ$  were not examined to avoid possible edge effects on film thickness. Figure 3c shows the spatial variation in the Ch-CNC film thickness. For the ISO-3 film,

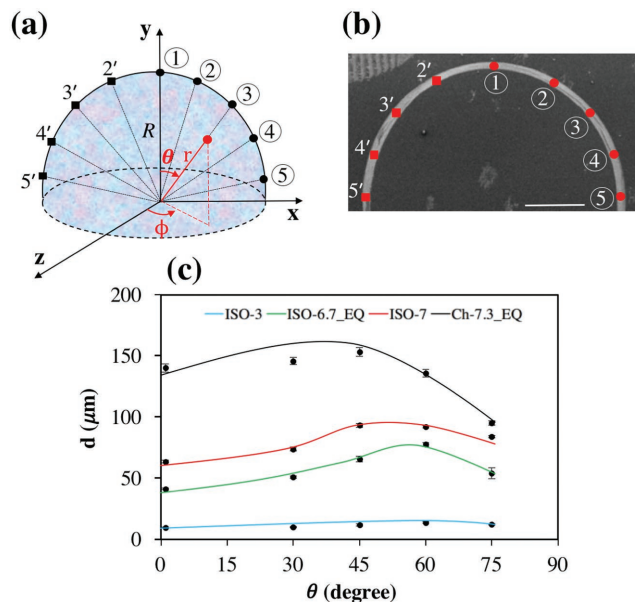


**Figure 3.** Variation in thickness of Ch-CNC films. a) Schematic illustration of the examined positions on the semi-spherical films. Positions 1–5 on the right half of the “cap” are located on the film surface at a radius  $r = R$  and an azimuthal angle  $\phi = 90^\circ$  with a varying polar angle  $\theta_1 = 0^\circ$ ,  $\theta_2 = 30^\circ$ ,  $\theta_3 = 45^\circ$ ,  $\theta_4 = 60^\circ$ , and  $\theta_5 = 75^\circ$ . Positions 2'–5' on the left half of the film are located on the film surface at  $r = R$  and an azimuthal angle  $\phi = 270^\circ$  with a varying polar angle  $\theta_{2'} = 30^\circ$ ,  $\theta_{3'} = 45^\circ$ ,  $\theta_{4'} = 60^\circ$ , and  $\theta_{5'} = 75^\circ$ , respectively. b) Representative scanning electron microscopy image of the cross-section of the ISO-7 film. The examined points are highlighted with red circles (right half of the film) and squares (left half of the film) on the SEM image. c) Variation in the film thickness,  $d$ , plotted versus  $\theta$  for the ISO-3, ISO-7, ISO-6.7\_EQ, and Ch-7.3\_EQ films. The lines are given for eye guidance. Each data point is an average taken over measurements at symmetric points on the film surface. The error bars represent standard deviation. The scale bar is 1 mm.

the evaporation of water resulted in the formation of a film with a uniform thickness of 11  $\mu\text{m}$ . The thickness of ISO-7, ISO-6.7\_EQ, and Ch-7.3\_EQ films was larger in the middle (at  $\theta_3 = 45^\circ$  or  $\theta_4 = 60^\circ$ ), in comparison with the film center ( $\theta_1 = 0^\circ$ ) and close-to-edge locations at  $\theta_5 = 75^\circ$ . More specifically, the thickness of the ISO-6.7\_EQ film of  $d \approx 77 \mu\text{m}$  at  $\theta_4 = 45^\circ$ , which was significantly larger than  $d$  of 41 and 54  $\mu\text{m}$  at  $\theta_1 = 0^\circ$  and  $\theta_5 = 75^\circ$ , respectively. As expected, the average film thickness increased with  $C_{\text{CNC}}$ .

### 3.3. Pitch Variation

Figure 4 shows the variation in  $P$  along the film surface on the right half of the curved Ch-CNC film. Figure 4a illustrates a schematic of the film cross-section with three examined positions 1–3 that were located at a radius  $r = R$  and an azimuthal angle  $\phi = 90^\circ$  with polar angles  $\theta_1 = 0^\circ$ ,  $\theta_2 = 45^\circ$ , and  $\theta_3 = 75^\circ$ , respectively. A multilayer “striped” structure was observed in the SEM images of all the curved films, similar to the morphology of planar Ch-CNC films.<sup>[18,41]</sup> Figure 4b shows representative SEM images of the cross-section of the ISO-3 film at positions 1–3. The half-pitch,  $P/2$  was measured as the distance between the layers in the SEM images. The spatial variation in  $P/2$  at the nominated points is shown in Figure 4c. Notably, the SEM images of a particular location of the ISO-7 and Ch-7.3\_EQ films exhibited regions with a large variability of  $P/2$  (Figure S5, Supporting Information). For the ISO-3 and ISO-6.7\_EQ films, the value of  $P/2$  for  $\theta_1 = 0^\circ$ ,  $\theta_2 = 45^\circ$ ,  $\theta_3 = 75^\circ$  reduced with  $C_{\text{CNC}}$ . Conversely, for the ISO-7 and Ch-7.3\_EQ films the value of  $P/2$  at positions 1–3 became larger, when  $C_{\text{CNC}}$  increased to 7 and 7.3 wt%. As shown

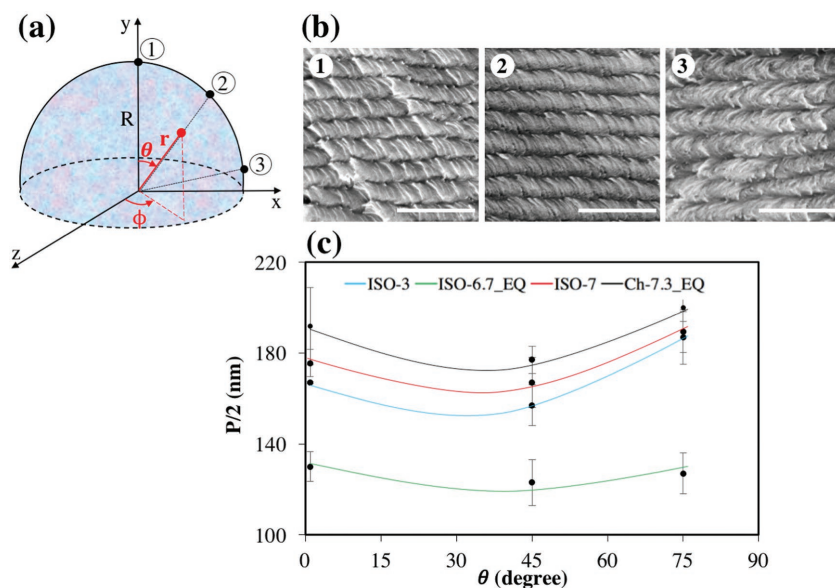


**Figure 4.** Variation in pitch in the Ch-CNC films. a) Schematic illustration of the film with indicated examined positions. b) SEM images of the cross-sectional area of the ISO-3 film at points 1, 2, and 3, corresponding to  $\theta_1 = 0^\circ$ ,  $\theta_2 = 45^\circ$ , and  $\theta_3 = 75^\circ$ , respectively (as illustrated in (a)). The scale bar is 1  $\mu\text{m}$ . c) Variation in pitch, plotted as a function of the polar angle  $\theta$  for the ISO-3, ISO-7, ISO-6.7\_EQ, and Ch-7.3\_EQ films. The lines are given for eye guidance. Every value of  $P$  is an average of ten measurements. The error bars represent the standard deviation.

in Figure 4c, the value of  $P/2$  for all the films was smaller at  $\theta_2 = 45^\circ$ , in comparison with those at  $\theta_1 = 0^\circ$  and  $\theta_3 = 75^\circ$ . Curved films with a radius  $R = 3 \text{ mm}$  showed a similar thickness and pitch variation along the film surface (Figure S6, Supporting Information).

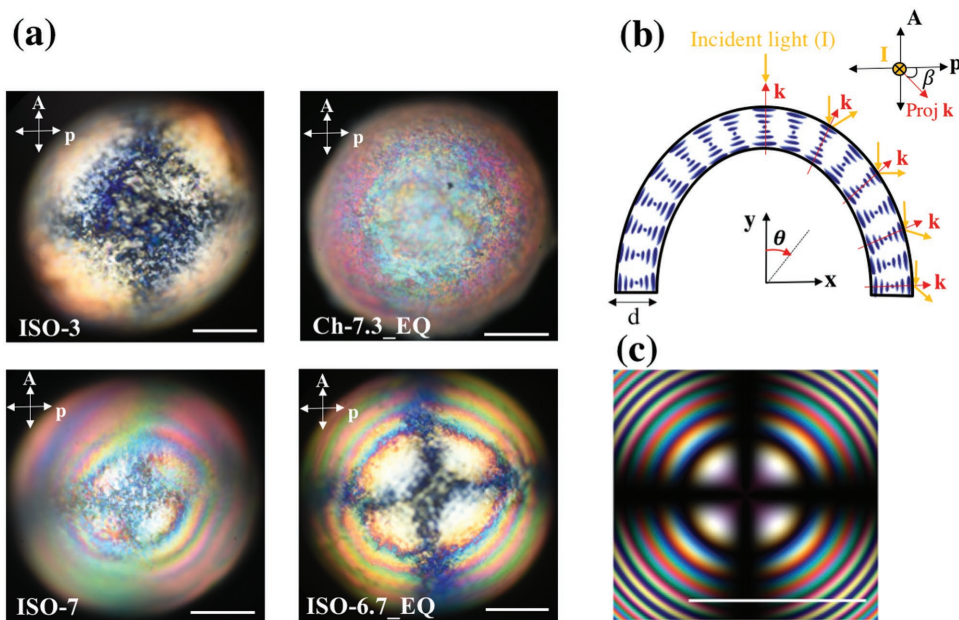
### 3.4. Film Texture

Figure 5a shows the characteristic polarizing optical microscopy (POM) textures of the curved Ch-CNC films that were examined in the transmission mode. The key features of these images can be summarized as follows. A clear Maltese cross was observed in the center of the POM images of the ISO-3 and ISO-6.7\_EQ films, corresponding to the radial CNC ordering at the film interface with the helical axis perpendicular to the surface, in agreement with the CNC planar anchoring at the CNCs-air interface.<sup>[42]</sup> For the ISO-7 film the Maltese cross was less pronounced. Second, close to the edges of the ISO-6.7\_EQ and ISO-7 films, we observed dark concentric rings with an average spacing of  $\approx 177 \mu\text{m}$ . Finally, films ISO-7 and Ch-7.3\_EQ exhibited a multicolor pattern, while two other films were close-to-monocolor. The POM images of the ISO-7 and Ch-7.3\_EQ films were qualitatively similar: both exhibited a mosaic pattern with a rainbow of blue, green, yellow, and pink colors close to the edges and with a relatively uniformly cyan-colored area close to the center.

The radially varying birefringence due to the helical director modulation in the spherical confinement has been previously demonstrated as the origin of the similar ring textures observed in transmission polarizing optical microscopy of short-pitch cholesteric shells.<sup>[43]</sup> The appearance of the Maltese cross and concentric rings at the edge of the curved Ch-CNC films can be explained as follows. When  $P$  is comparable or smaller than the wavelength of light used for the observation, the optical properties of the Ch layers can be represented by an effective medium response,<sup>[44]</sup> which is similar to a nematically ordered layer with the ordering direction along helical axis,  $k$ . In our work, the measured values of  $P$  of the Ch-CNC films were smaller than the wavelength of broadband visible light used to obtain the crosspolarized images shown in Figure 5. Under crossed polarizers, the variations of the intensity of light ( $I$ ) transmitted through the Ch-CNC films can be expressed as<sup>[45]</sup>

$$I \propto \sin^2(2\beta) \sin^2(\Delta n_{\text{eff}} d_{\text{eff}} \pi / \lambda) \quad (1)$$

where  $\beta$  is the angle between the polarizer  $p$  and projection of helical axis  $k$  in the plane perpendicular to the incident light,  $\Delta n_{\text{eff}}$  and  $d_{\text{eff}}$  are the effective birefringence and effective thickness of the CNC film, respectively, and  $\lambda$  is the wavelength of light used for imaging. At  $\theta = 0^\circ$ , the helical axis of the Ch layers is aligned parallel to the incident light, and the central region of the film appears dark in the POM images. However, at  $\theta > 0^\circ$  the curved



**Figure 5.** a) Polarized optical microscopy images of curved ISO-3, ISO-7, ISO-6.7\_EQ, and Ch-7.3\_EQ films. b) Illustration of the cross-section of a Ch-CNC film. c) Computer-simulated crosspolarized image of the ISO-7 film.  $k$  represents the axis of helix and  $\beta$  is the angle between the polarizer  $p$  and projection of helical axis  $k$  into a plane perpendicular to the incident light. Film radius is 2 mm. All scale bars are 1 mm.

film regions were birefringent ( $\Delta n_{\text{eff}} < 0$ ), owing to the inclination of the helical axis with respect to the illumination light (see Figure 5b). In this case, the film regions with the projection of helical axis  $k$  into a plane perpendicular to the incident light aligned parallel ( $\beta = 0$ ) or perpendicular ( $\beta = 90$ ) to the polarizer  $p$  (see Figure 5b inset) appeared dark, thus resulting in the Maltese cross (Figure 5). The gradual increase in  $\Delta n_{\text{eff}}$  and  $d_{\text{eff}}$  of the Ch-CNC film, from  $\theta = 0^\circ$  to  $\theta = 90^\circ$  (see Figure 5) resulted in the polarized interference pattern close to the film edges, where conditions ( $\Delta n_{\text{eff}} d_{\text{eff}} \pi / \lambda = n\pi$ ) were satisfied and resulted in dark regions in the POM images. Due to the spherical symmetry of the Ch-CNC films, these regions were concentric, as shown in Figure 5a. Using Equation (1), we simulated a crosspolarized image for an ideal curved CNC film, in which the helical axis is perpendicular to the plane of the surface at each point on the film. The simulated image exhibited a Maltese cross and interference fringes (Figure 5c), closely agree with the experimentally observed POM image of ISO-7 and ISO-6.7\_EQ depicted in Figure 5a.<sup>[43]</sup> The POM images of the ISO-7 and ISO-6.7\_EQ films were close to the simulated image; however, some degrees of disorder in these films resulted in the lower intensity Maltese cross. Notably the Maltese cross and interference fringes were not observed in the Ch-7.2\_EQ film (see Section 4). The POM images of the Ch-CNC films with a radius  $R = 3$  mm exhibited textures and concentric rings identical to those observed in the curved films with the radius  $R = 2$  mm (Figure S7, Supporting Information).

### 3.5. Optical Properties of Ch-CNC Films

Figure 6 shows reflectance spectra of the Ch-CNC films, which were measured at the normal incidence and for the reflection

angle of  $90^\circ$  at positions 1–3 at  $\theta_1 = 0^\circ$ ,  $\theta_2 = 45^\circ$ , and  $\theta_3 = 75^\circ$ , respectively, as shown in Figure 4a. The reflectance spectra of the Ch-CNC films that were measured for the inner and the outer surfaces were identical, thus indicating a minor effect of the PDMS substrate and its surface interaction with CNCs during water evaporation. At  $\theta_1 = 0^\circ$ , the reflection intensity and bandwidth of the reflectance peak for the ISO-7 and Ch-7.3\_EQ films were significantly greater than that of the ISO-3 and ISO-6.7\_EQ films. The difference in peak intensity could be ascribed to a larger thickness of the ISO-7 and Ch-7.3\_EQ films (see Figure 4c).<sup>[28]</sup> For all the films, the reflection peak in the center of the film ( $\theta_1 = 0^\circ$ ) had a lower intensity than the peak at the middle and edges of the film ( $\theta_2 = 45^\circ$  and  $\theta_3 = 75^\circ$ , respectively). This effect can be linked to the inclination of the helix, as reflectivity of the film depends on the helix angle; for incident light parallel to the helical axis there is only one band of selective reflection, while for obliquely incident light series of higher order reflection bands occur. Moreover, in the film region with large oblique incidence, total reflection occurs, thereby effectively increasing the overall reflectance intensity.<sup>[46]</sup>

For the center and edge of the ISO-7 and Ch-7.3\_EQ films, broadband reflection was measured, explaining the “metallic” appearance of these films (Figure 2). The peak wavelength for these films showed redshift, in comparison with ISO-3 and ISO-6.7\_EQ films, and in agreement with the measured pitch (Figure 4c). A lower reflection intensity was measured for the edge of the Ch-7.3\_EQ film than for the corresponding position of the ISO-7. Moreover, the peak wavelength for the ISO-7 and Ch-7.3\_EQ films at the position of  $\theta_2 = 45^\circ$  redshifted from the peak position expected from the pitch profile shown in Figure 4c (the minimum value of  $P$  for all the films was measured at the position of  $\theta_2 = 45^\circ$ ). This reflectance peak deviation from the typical  $P$  values is caused by the helical axis tilt and

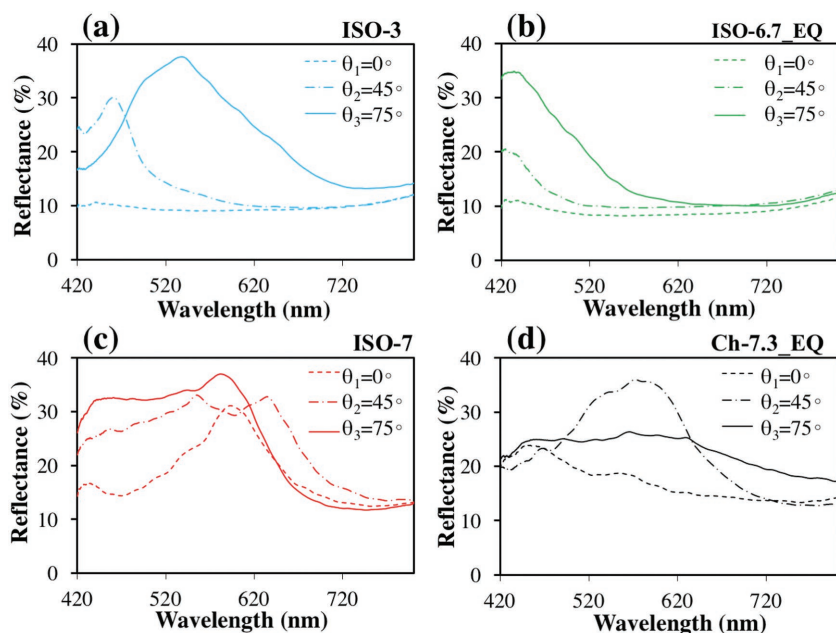


**Figure 6.** Reflection spectra of the curved Ch-CNC films in the center ( $\theta_1 = 0^\circ$ ), middle ( $\theta_2 = 45^\circ$ ), and edge ( $\theta_3 = 75^\circ$ ) at the normal angle of incidence and for the reflection angle of  $90^\circ$ . a) ISO-3, b) ISO-7, c) ISO-6.7\_EQ, and d) Ch-7.3\_EQ films.

local disorder. Similar reflection spectra were acquired for the curved films with a radius  $R = 3$  mm (Figure S8, Supporting Information).

To highlight the role of curvature on the optical properties of the curved Ch-CNC films, we investigated the optical responses of the planar films fabricated from the CNC suspensions listed in Table 1. **Figure 7a** shows the characteristic POM textures of the planar Ch-CNC films. While a planar P-ISO-3 film exhibited a white marble-like texture with a trace of cyan color, three other planar films showed a similar mosaic pattern with a blue color close to the film edge and a rainbow of yellow, pink, and green colors in the film center. The P-Ch-6.7\_EQ film exhibited

less intense colors, in comparison with P-ISO-7 and P-Ch-7.3\_EQ films.

**Figure 7b** shows the corresponding reflectance spectra of the planar films, measured at the normal incidence by UV-vis spectroscopy. The P-ISO-3 film exhibited a low-intensity reflectance peak at a wavelength of  $\approx 600$  nm. The P-ISO-7, P-Ch-6.7\_EQ, and P-Ch-7.3\_EQ films showed the reflectance peak centered at  $\approx 550$  nm. As expected, the reflection from the planar P-Ch-7.3\_EQ film was more intense and covered a broader spectrum range, compared to the P-ISO-7 and P-Ch-6.7\_EQ films.

#### 4. Discussion

The variation in the thickness, texture, structure, and optical properties of the Ch-CNC films was governed by three factors: the composition of the precursor CNC suspension, their state (that is, isotropic vs liquid crystalline), and film curvature. As shown in Table 1, the CNC suspensions used for the preparation of the ISO-3, ISO-6.7\_EQ, ISO-7, and Ch-7.3\_EQ films exhibited the corresponding increase in viscosity. Second, for the first three suspensions the evaporation of water led to the appearance of tactoids; however, the suspension used for the preparation of the Ch-7.3\_EQ contained an equilibrated Ch phase.

For the ISO-3 and ISO-6.7\_EQ films obtained from the CNC suspensions with lower viscosity, the value of  $P$  at three examined positions in the films reduced with  $C_{\text{CNC}}$  increasing from 3 to 6.7 wt% (Figure 4). This effect was in agreement with previous reports for planar films<sup>[47]</sup> and was ascribed to the reduced electrostatic repulsion between CNCs at a higher  $C_{\text{CNC}}$ .<sup>[48]</sup> Conversely, for the ISO-7 and Ch-7.3\_EQ films, the

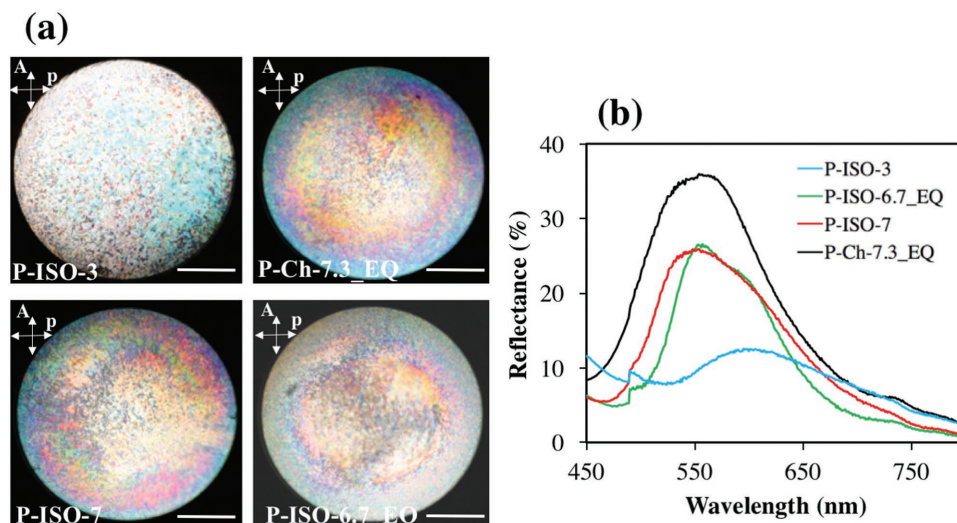


**Figure 7.** a) Polarized optical microscopy images of planar ISO-3, ISO-7, ISO-6.7\_EQ, and Ch-7.3\_EQ films. The scale bars are 2 mm. b) Reflection spectra of the corresponding films  $R = 3$  mm.

value of  $P$  at three examined film positions increased when  $C_{\text{CNC}}$  increased to 7 and 7.3 wt%. We attribute this effect to the higher viscosity of the precursor CNC suspensions: the CNC motion was restricted during their evaporation-induced self-assembly, due to the formation of a gel and the corresponding kinetic arrest of Ch-CNC structure.<sup>[18]</sup>

For the same reason, the texture of the ISO-7 and Ch-7.3\_EQ films was represented by the multicolor mosaic pattern, while the ISO-3 and ISO-6.7\_EQ films prepared from the lower viscosity suspensions showed nearly a single color. The multicolor texture of ISO-7 and Ch-7.3\_EQ films was governed by the existence of regions with a different orientation of helical axes and a variation in  $P$  (see Figures S5 and S9, Supporting Information).<sup>[49]</sup> We conclude that higher viscosity of the precursor suspensions caused the restricted mobility of the CNCs,<sup>[18,39]</sup> which being coupled with a semi-spherical geometry of the drying films (*see below*) caused distortions in the Ch structure, thus resulting in the variation in  $P$  and helical axis inclination. This effect was also leading to the broadening of the reflectance bands of the ISO-7 and Ch-7.3\_EQ films, compared to the ISO-3 and ISO-6.7\_EQ films (Figure 6). We stress however that although the viscosities of the suspensions used for the preparation of the ISO-7 and Ch-7.3\_EQ films are comparable, their POM textures and optical responses were distinct: the Ch-7.3\_EQ film did not exhibit the Maltese cross compared to the ISO-7 film. This effect was ascribed to the different states of the precursor suspensions. The Ch state of the suspension used for the preparation of Ch-7.3\_EQ films promoted gel formation and the corresponding kinetic arrest of the multidomain Ch-CNC structure upon drying.<sup>[18]</sup>

The role of curvature on the structure of the Ch-CNC films manifested itself in the variation in thickness and pitch from the edge to the center of the film. The thickness of the ISO-7, ISO-6.7\_EQ, and Ch-7.3\_EQ films was larger in the middle of the film, in comparison with its center and edges (Figure 3). The value of  $P$  for all the films was smaller in the middle of the film in comparison with its center and edges (Figure 4). The location of the minimum value of  $P$  was in agreement with the greater CNC deposition upon drying: the greater was the film thickness the smaller was  $P$ . We ascribe this dependence to the dynamic forces acting in the CNC suspension that was drying in a semi-spherical geometry (*see Figure S10, Supporting Information*). These forces play a key role in the modulation of film thickness, similar to the effects observed for evaporating droplets of colloidal suspensions.<sup>[26,50]</sup> Upon drying, the CNCs flow outward from the center ( $\theta = 0^\circ$ ) to the edges ( $\theta = 90^\circ$ ) of the liquid layer, due to the capillary force, in order to compensate for the stronger evaporation of water at the contact line.<sup>[26]</sup> This flow results in a higher surface tension at the contact line<sup>[51]</sup> and therefore, creates an inward flow toward the film center (the Marangoni flow).<sup>[50b]</sup> Thus the location of the greater deposition of CNCs (higher thickness) is influenced by the balance between gravity, capillary flow, and Marangoni flow.<sup>[52]</sup> In contrast, in planar Ch-CNC films the CNCs mostly deposit close to the film edges, due to the dominant role of capillary flow and as a result the modulation in film thickness exhibit a different profile than in the semi-spherical films, as shown in Figure S11 in the Supporting

Information and Figure 3c, respectively. Moreover, as the POM images of the same-composition planar CNC films exhibited neither the ring patterns, nor a clear Maltese cross (Figure 7a), we conclude that the semi-spherical geometry promotes the radial configuration of the liquid crystal with planar anchoring, thus giving rise to the Maltese cross and interference fringes (particularly, for the films formed from low-viscosity suspensions). Preparation of the same films in the planar geometry resulted in unidirectional helicoidal structures, with a helical axis oriented vertically to the substrate. Finally, due to the competition of dynamic forces film formation in the semi-spherical geometry resulted in a pronounced broadband reflection, especially, for the films formed from suspensions with high viscosity, compared with the narrow band reflection in the corresponding planar Ch-CNC films (Figure 7b). Thus the fabrication of curved Ch-CNC film is an efficient strategy to the broadening the reflection bandwidth, in comparison with the proposed approach to such films using multiple layers with gradient pitch.<sup>[31b]</sup>

## 5. Conclusions

We have fabricated Ch-CNC photonic semi-spherical films from CNC suspensions with different compositions, structures, and viscosities. The films formed by low-viscous isotropic suspensions yielded films with a radial CNC organization and a single, narrow-band reflection. Films formed from the concentrated nonequibrated isotropic and the equilibrated suspensions yielded Ch-CNC films with a polydomain morphology and a broadband reflection covering the entire spectral range. Film thickness, structure, and optical properties changed along the film surface: from the edge to the center of the film, which was ascribed to the dynamic forces acting during the drying of CNC suspension confined in semi-spherical geometry. Coupling of the effect of the composition and Ch state of the CNC suspensions with their spherical geometry enabled simple and effective preparation of the Ch-CNC films with broadband reflection, thus overcoming the narrow-band reflection of planar Ch-CNC films, a major limitation in the fabrication of broadband reflectors, and circular polarizers. This work provides guidance for the fabrication of curved Ch-CNC films with predesigned structure and optical properties.

## 6. Experimental Section

**Materials:** Poly(dimethylsiloxane) (PDMS) elastomer base and curing agent (Sylgard 184) was supplied by Dow Corning. An aqueous 12 wt% suspension of CNCs carrying surface sulfate half-ester groups was purchased from the University of Maine Process Development Center. Milli-Q water was used to prepare CNC suspensions with concentrations,  $C_{\text{CNC}}$ , of 3 and 7 wt%. A pristine CNC suspension was diluted with deionized water to prepare isotropic suspensions with  $C_{\text{CNC}}$  of 3 or 7 wt%, which were used to obtain films ISO-3 and ISO-7, respectively. Films ISO-6.7\_EQ and Ch-7.3\_EQ with  $C_{\text{CNC}}$  of 6.7 and 7.3 wt%, respectively, were prepared in the following way. A portion of the CNC suspension with  $C_{\text{CNC}}$  of 7.0 wt% was allowed to equilibrate in a sealed glass vial for 21 d. The suspension phase-separated into

a top isotropic and a bottom Ch phase with  $C_{\text{CNC}}$  of 6.7 and 7.3 wt%, respectively. The volume fraction of the top isotropic phase in this two-phase system was 0.48, which is in agreement with the earlier reports.<sup>[53]</sup> Following phase equilibration, the top and bottom phases were separated using a micropipette, and each of these phases was used for film preparation.

**Film Characterization:** The photographs of the semi-spherical Ch-CNC films placed against the black background were acquired using a Nikon D7200 camera. The POM images of the films were acquired on an optical microscope (Olympus BX51) in the transmission mode using a Nikon D7200 camera. SEM imaging of the curved Ch-CNC films were acquired using Quanta field electron and ion company (FEI) Scanning Electron Microscope (FEG 250). Prior to imaging, the films were freeze fractured in liquid nitrogen and subsequently coated with gold using a SC7640 High Resolution Sputter Coater (Quorum Technologies) for 30 s at 2.0 kV. For thickness measurement, semi-spheres were embedded into blocks of Spurr epoxy resin (Spurr Low Viscosity Embedding Kit, Sigma) and were polished/sectioned using a diamond knife on an Ultracut E ultra-microtome at cutting speed = 1.0 mm s<sup>-1</sup>, knife angle = 45°, and clearance angle of 6°.

The reflectance measurements of the curved Ch-CNC films were performed on an inverted microscope (Olympus IX 71). The samples were illuminated with a parallel beam of light from a white light source using a 20 × objective (Olympus, SLMPlan). The reflected light from the sample was collected by the same objective and guided to a spectrometer (Ocean optics, USB 2000-FLG) using an optical fiber. Reflectance at different locations along the curved Ch-CNC films surfaces was characterized by bringing a specific area into focus by tilting the sample while keeping the illuminated area normal to the incident light. Extinction spectra of the planar CNC films were acquired using a Varian Cary 5000 UV-vis-NIR spectrophotometer. The films were placed orthogonally to the incident beam with a reflection area of 30 mm<sup>2</sup>. The viscosities of the CNC suspensions were measured using Discovery-HR-1 hybrid rheometer (TA instruments) with a cone and plate geometry at a cone nominal angle ≈ 1° and cone diameter of 40 mm. All the suspensions were tested at 25 °C and at a strain of 1%. The contact angles of CNC dispersion droplets were measured using the Kruss tensiometer (DSA100). Surface treatment of the PDMS molds were carried out using the PDC-32G plasma cleaner (Harrick Plasma, USA).

## Supporting Information

Supporting Information is available from the Wiley Online Library or from the author.

## Acknowledgements

E.K. thanks Connaught Foundation and The Natural Sciences and Engineering Research Council of Canada (NSERC) (Discovery and Strategic grants) for financial support of this work. P.R. thanks Fonds de recherche du Québec – Nature et technologies (FRQNT) Postdoctoral Research Scholarship. M.A. thanks Vanier Canada Graduate Scholarship. I.I.S. and H.M. acknowledge the support of the U.S. Department of Energy, Office of Basic Energy Sciences, Division of Materials Sciences and Engineering, under award ER46921, contract DE-SC0010305 with the University of Colorado at Boulder. The authors thank I. Gourevich (Centre for Nanostructure Imaging) for assistance in electron microscopy imaging, B. Calvieri and S. Doyle from Microscopy Imaging Lab at Faculty of Medicine at University of Toronto for electron microscopy sample preparation, and N. Khuu for assistance in rheology experiments. The authors thank Dr. A. Khabibullin, B. Senyuk, Q. Liu, and S. Park for fruitful discussions.

## Conflict of Interest

The authors declare no conflict of interest.

## Keywords

broadband reflection, cellulose nanocrystals, cholesteric liquid crystals, curved chiral film

Received: June 4, 2018

Revised: August 7, 2018

Published online: September 14, 2018

- [1] F. Livolant, A. Leforestier, *Prog. Polym. Sci.* **1996**, *21*, 1115.
- [2] M. M. Giraudguille, *Calcif. Tissue Int.* **1988**, *42*, 167.
- [3] E. Belamie, G. Mosser, F. Gobeaux, M. M. Giraud-Guille, *J. Phys.: Condens. Matter* **2006**, *18*, 115.
- [4] M. A. Meyers, P. Y. Chen, A. Y. M. Lin, Y. Seki, *Prog. Mater. Sci.* **2008**, *53*, 1.
- [5] E. A. Zimmermann, B. Gludovatz, E. Schaible, N. K. N. Dave, W. Yang, M. A. Meyers, R. O. Ritchie, *Nat. Commun.* **2013**, *4*, 2634.
- [6] W. Yang, V. R. Sherman, B. Gludovatz, E. Schaible, P. Stewart, R. O. Ritchie, M. A. Meyers, *Nat. Commun.* **2015**, *6*, 6649.
- [7] Y. Bar-Cohen, *Biomimetics: Nature-Based Innovation*, CRC Press, Boca Raton, FL **2012**.
- [8] a) S. Vignolini, P. J. Rudall, A. V. Rowland, A. Reed, E. Moyroud, R. B. Faden, J. J. Baumberg, B. J. Glover, U. Steiner, *Proc. Natl. Acad. Sci. USA* **2012**, *109*, 15712; b) D. W. Lee, J. B. Lowry, *Nature* **1975**, *254*, 50.
- [9] V. Sharma, M. Crne, J. O. Park, M. Srinivasarao, *Science* **2009**, *325*, 449.
- [10] S. Vignolini, T. Gregory, M. Kolle, A. Lethbridge, E. Moyroud, U. Steiner, B. J. Glover, P. Vukusic, P. J. Rudall, *J. R. Soc. Interface* **2016**, *13*, 20160645.
- [11] M. Hernandez-Jimenez, D. E. Azoifeifa, E. Libby, C. Barboza-Aguilar, A. Solis, L. Arce-Marengo, I. Garcia-Aguilar, A. Hernandez, W. E. Vargas, *Opt. Mater. Express* **2014**, *4*, 2632.
- [12] A. G. Dumanli, T. Savin, *Chem. Soc. Rev.* **2016**, *45*, 6698.
- [13] H. M. Whitney, M. Kolle, P. Andrew, L. Chittka, U. Steiner, B. J. Glover, *Science* **2009**, *323*, 130.
- [14] M. D. Shawkey, N. I. Morehouse, P. Vukusic, *J. R. Soc. Interface* **2009**, *6*, S221.
- [15] a) S. N. Fernandes, Y. Geng, S. Vignolini, B. J. Glover, A. C. Trindade, J. P. Canejo, P. L. Almeida, P. Brogueira, M. H. Godinho, *Macromol. Chem. Phys.* **2013**, *214*, 25; b) M. Kolle, P. M. Salgard-Cunha, M. R. J. Scherer, F. M. Huang, P. Vukusic, S. Mahajan, J. J. Baumberg, U. Steiner, *Nat. Nanotechnol.* **2010**, *5*, 511; c) J. M. Slocik, S. Tadepalli, M. K. Gupta, R. R. Naik, S. Singamaneni, *Chem. Rev.* **2017**, *117*, 12705; d) M. Kolle, S. Lee, *Adv. Mater.* **2018**, *30*, 1702669.
- [16] Y. P. Zhang, V. P. Chodavarapu, A. G. Kirk, M. P. Andrews, *Sens. Actuators, B* **2013**, *176*, 692.
- [17] J. P. F. Lagerwall, C. Schutz, M. Salajkova, J. Noh, J. H. Park, G. Scalia, L. Bergstrom, *NPG Asia Mater.* **2014**, *6*, 80.
- [18] a) K. E. Shopsowitz, W. Y. Hamad, M. J. MacLachlan, *J. Am. Chem. Soc.* **2012**, *134*, 867; b) D. Gray, *Nanomaterials* **2016**, *6*, 213.
- [19] G. von Freymann, V. Kitaev, B. V. Lotsch, G. A. Ozin, *Chem. Soc. Rev.* **2013**, *42*, 2528.
- [20] J. T. Woolley, *Plant Physiol.* **1975**, *55*, 172.
- [21] H. Devries, *Acta Crystallogr.* **1951**, *4*, 219.
- [22] Y. P. Zhang, V. P. Chodavarapu, A. G. Kirk, M. P. Andrews, *J. Nanophotonics* **2012**, *6*, 1.
- [23] J. Majoinen, J. Hassinen, J. S. Haataja, H. T. Rekola, E. Kontturi, M. A. Kostianen, R. H. A. Ras, P. Torma, O. Ikkala, *Adv. Mater.* **2016**, *28*, 5262.
- [24] P. L. Almeida, S. Kundu, J. P. Borges, M. H. Godinho, J. L. Figueirinhas, *Appl. Phys. Lett.* **2009**, *95*, 043501.
- [25] R. Xiong, A. M. Grant, R. L. Ma, S. D. Zhang, V. V. Tsukruk, *Mater. Sci. Eng., R* **2018**, *125*, 1.



- [26] A. Gencer, C. Schutz, W. Thielemans, *Langmuir* **2017**, *33*, 228.
- [27] T. D. Nguyen, W. Y. Hamad, M. J. MacLachlan, *Chem. Commun.* **2013**, *49*, 11296.
- [28] D. G. Liu, S. Wang, Z. S. Ma, D. L. Tian, M. Y. Gu, F. Y. Lin, *RSC Adv.* **2014**, *4*, 39322.
- [29] H. K. Bisoyi, T. J. Bunning, Q. Li, *Adv. Mater.* **2018**, *30*, 1706512.
- [30] a) H. Therien-Aubin, A. Lukach, N. Pitch, E. Kumacheva, *Nanoscale* **2015**, *7*, 6612; b) R. Bardet, N. Belgacem, J. Bras, *ACS Appl. Mater. Interfaces* **2015**, *7*, 4010; c) G. Guidetti, S. Atifi, S. Vignolini, W. Y. Hamad, *Adv. Mater.* **2016**, *28*, 10042.
- [31] a) J. K. Gansel, M. Thiel, M. S. Rill, M. Decker, K. Bade, V. Saile, G. von Freymann, S. Linden, M. Wegener, *Science* **2009**, *325*, 1513; b) M. Mitov, *Adv. Mater.* **2012**, *24*, 6260.
- [32] a) M. Humar, I. Musevic, *Opt. Express* **2010**, *18*, 26995; b) Y. Uchida, Y. Takanishi, J. Yamamoto, *Adv. Mater.* **2014**, *26*, 4919.
- [33] J. Noh, H. L. Liang, I. Drevensek-Olenik, J. P. F. Lagerwall, *J. Mater. Chem. C* **2014**, *2*, 806.
- [34] Y. Geng, J. Noh, I. Drevensek-Olenik, R. Rupp, G. Lenzini, J. P. F. Lagerwall, *Sci. Rep.* **2016**, *6*, 26840.
- [35] R. J. Hernandez, A. Mazzulla, A. Pane, K. Volke-Sepulveda, G. Cipparrone, *Lab Chip* **2013**, *13*, 459.
- [36] a) Y. F. Li, J. J. Y. Suen, E. Prince, E. M. Larin, A. Klinkova, H. Therien-Aubin, S. J. Zhu, B. Yang, A. S. Helmy, O. D. Lavrentovich, E. Kumacheva, *Nat. Commun.* **2016**, *7*, 12520; b) P. X. Wang, W. Y. Hamad, M. J. MacLachlan, *Angew. Chem., Int. Ed.* **2016**, *55*, 12460.
- [37] S. H. Cho, Y. F. Li, M. Seo, E. Kumacheva, *Angew. Chem., Int. Ed.* **2016**, *55*, 14014.
- [38] R. M. Parker, B. Frka-Petesic, G. Guidetti, G. Kamita, G. Consani, C. Abell, S. Vignolini, *ACS Nano* **2016**, *10*, 8443.
- [39] F. Jativa, C. Schutz, L. Bergstrom, X. H. Zhang, B. Wicklein, *Soft Matter* **2015**, *11*, 5374.
- [40] S. H. Tan, N. T. Nguyen, Y. C. Chua, T. G. Kang, *Biomicrofluidics* **2010**, *4*, 32204.
- [41] J. Majoinen, E. Kontturi, O. Ikkala, D. G. Gray, *Cellulose* **2012**, *19*, 1599.
- [42] R. M. Parker, G. Guidetti, C. A. Williams, T. Zhao, A. Narkevicius, S. Vignolini, B. Frka-Petesic, *Adv. Mater.* **2017**, *30*, 1704477.
- [43] Y. Geng, J. H. Noh, J. P. F. Lagerwall, *Proc. SPIE, Emerging Liquid Crystal Technologies XI* **2016**, *9769*, 15.
- [44] a) C. Oldano, M. Rajteri, *Phys. Rev. B* **1996**, *54*, 10273; b) J. A. De La Cruz, Q. Liu, B. Senyuk, A. W. Frazier, K. Peddireddy, I. I. Smalyukh, *ACS Photonics* **2018**, *5*, 2468.
- [45] P. Yeh, C. Gu, *Optics of Liquid Crystal Displays*, Wiley, New York **1999**.
- [46] a) R. Dreher, G. Meier, *Phys. Rev. A* **1973**, *8*, 1616; b) H. Takezoe, Y. Ouchi, M. Hara, A. Fukuda, E. Kuze, *Jpn. J. Appl. Phys., Part 1* **1983**, *22*, 1080.
- [47] a) C. Schutz, M. Agthe, A. B. Fall, K. Gordeyeva, V. Guccini, M. Salajkova, T. S. Plivelic, J. P. F. Lagerwall, G. Salazar-Alvarez, L. Bergstrom, *Langmuir* **2015**, *31*, 6507; b) S. Beck-Candanedo, M. Roman, D. G. Gray, *Biomacromolecules* **2005**, *6*, 1048; c) E. Belamie, P. Davidson, M. M. Giraud-Guille, *J. Phys. Chem. B* **2004**, *108*, 14991.
- [48] Y. Habibi, L. A. Lucia, O. J. Rojas, *Chem. Rev.* **2010**, *110*, 3479.
- [49] A. G. Dumanli, H. M. van der Kooij, G. Kamita, E. Reisner, J. J. Baumberg, U. Steiner, S. Vignolini, *ACS Appl. Mater. Interfaces* **2014**, *6*, 12302.
- [50] a) C. N. Kaplan, L. Mahadevan, *J. Fluid Mechanics* **2015**, *781*, R2; b) G. Chu, R. Vilensky, G. Vasilyev, P. Martin, R. Zhang, E. Zussman, *J. Phys. Chem. Lett.* **2018**, *9*, 1845.
- [51] H. Hu, R. G. Larson, *J. Phys. Chem. B* **2006**, *110*, 7090.
- [52] B. J. Fischer, *Langmuir* **2002**, *18*, 60.
- [53] E. E. Urena-Benavides, G. Y. Ao, V. A. Davis, C. L. Kitchens, *Macromolecules* **2011**, *44*, 8990.